RSC Advances

PAPER

View Article Online
View Journal | View Issue

Cite this: *RSC Adv.*, 2025, **15**, 21639

Synergistic effects of sewage sludge ash and limestone in cement-based composites: hydration kinetics and mechanical performance†

Zhiyang Chang, [a] Huimin Wang,[a] Hongzhi Yue,[a] Huijun Xu[b] and Dongming Liu*[a]

The use of solid waste as a supplementary cementitious material (SCM) has the potential to reduce CO_2 emissions in the cement industry. Sewage sludge ash (SSA), generated during the incineration of municipal wastewater treatment residues, has emerged as a viable SCM candidate for fabricating ternary cementitious systems incorporating cement and limestone. This study systematically investigated the hydration kinetics, phase evolution, and mechanical behavior of SSA-modified ternary composites. The research particularly focused on elucidating the synergistic interactions between SSA components and conventional cement hydrates under different compositions of ternary composites. Experimental results showed that fine SSA particles provided crystal nuclei for the crystallization and precipitation of hydration products and further increased the initial release of hydration heat. Besides, the reactive aluminate and silicate in SSA facilitated its reaction with limestone and the formation of aluminum-containing hydrates and carboaluminate phases. The formation of additional ettringite was also observed when the gypsum content was increased. These additional hydrates filled in the large capillary pores of hardened cement paste, resulting in a denser microstructure and higher compressive strength. The ternary composite incorporating 20% SSA, 10% limestone and 2% gypsum exhibited a compressive strength of 49.54 MPa with a strength activity index (SAI) of 94.56% at 28 days. The excellent mechanical performance of this ternary composite demonstrates its significant potential for the development of low-carbon cementitious materials.

Received 4th April 2025
Accepted 11th June 2025

DOI: 10.1039/d5ra02341f

rsc.li/rsc-advances

1 Introduction

The cement industry is one of the foremost energy consumers and CO_2 emitters today, contributing to 6–8% global anthropogenic carbon emissions every year.[1] As one of the world's largest cement manufacturers and consumers, China is confronted with transformational challenges to reduce its CO_2 emissions in line with its ambition to achieve carbon neutrality.[2] Existing mitigation measures in the cement industry include changes in fuel usage,[3] cement substitution,[4] and carbon capture, utilization and storage (CCUS).[5,6] It has been estimated that cement substitution with supplementary cementitious materials could reduce 44% of the annual global CO_2 emissions from cement production and is consequently regarded as one of the most promising approaches for reducing CO_2 emissions.[7] Limestone calcined clay cement (LC^3) technology offers an alternative for the partial substitution of cement with calcined clay and limestone. Notwithstanding the advantages of employing LC^3 technology in the manufacture of building materials, such as excellent mechanical strength and durability, the massive consumption of natural clay sources still gives rise to a contradiction from a sustainability perspective.[8–10] Further research on solid wastes possessing similar properties to clay utilized as mineral additions is thus recommended.

Sewage sludge is a by-product produced from the wastewater treatment process, consisting of a significant amount of organic materials along with diverse bacteria and microorganisms. In China, conventional disposal methods such as sanitary landfilling and agricultural application have faced increasingly stringent limitations due to environmental protection regulations. Incineration is regarded as one of the most environmentally sustainable approaches for the disposal of sewage sludge, owing to its benefits in reducing the sludge volume and eliminating hazardous components.[11,12] Nevertheless, substantial quantities of residual ash produced during the incineration process are predominantly disposed of in landfills, resulting in secondary environmental pollution.[13] Consequently, there is an urgent need for the effective disposal and utilization of sewage sludge ash (SSA). SSA possesses a comparable oxide composition to that of calcined clay, including SiO_2, Al_2O_3 and CaO,

[a]*School of Materials Science and Engineering, Shandong University of Technology, Zibo, Shandong 255000, China. E-mail: dmliu2015@126.com*

[b]*School of Chemistry and Chemical Engineering, Shandong University of Technology, Zibo, Shandong 255000, China*

† Electronic supplementary information (ESI) available. See DOI: https://doi.org/10.1039/d5ra02341f

which endows it with the potential to function as a supplementary cementitious material in concrete production.[14,15]

The potential application of SSA in the production of building materials has been extensively investigated in many studies.[16–18] The impact of SSA on the properties of cement-based materials can be ascribed to mechanisms such as nucleation, physical filling, chemical reactions, and dilution. When the dosage of SSA is below 10%, the finely pulverized ash particles can provide a greater number of nucleation sites for the hydration products of cement clinkers, thereby accelerating the early hydration of the clinkers.[19] Also, the size of milled SSA particles is smaller than that of cement particles, thereby optimizing particle packing and the distribution of pore sizes in the cement paste. Consequently, an enhancement in early strength is achieved for cement-based materials.[20] However, when the dosage of sludge ash exceeds 20%, the water demand of the blended cement slurry increases, leading to a significant reduction in its workability, attributed to the high specific surface area and porous structure of SSA particles.[21] Over time, both the physical filling effect and chemical interactions of SSA are insufficient to offset the strength deterioration caused by the dilution effects in the cement paste, resulting in a decrease in the compressive strength.[22] The chemical reactions of SSA are related with its pozzolanic activity, albeit this remains a topic of debate. Some researchers have reported that the strength activity index (SAI) of SSA can reach to 70% or even exceed 85%, classifying it as a highly pozzolanic material.[23] However, other scholars have argued against its pozzolanic activity based on Frattini test results.[24] The controversy arises somewhat due to variations in the sludge composition, incineration processes, and methods for evaluating the pozzolanic activity. With advancements in wastewater treatment technology, aluminum-rich flocculants have supplanted lime in the dehydration process of sewage sludge, leading to an increased aluminum content in dehydrated sewage sludge, subsequently affecting the pozzolanic activity of SSA. For instance, phosphorus-bearing substances in SSA could react with portlandite to form poor crystallinity hydroxyapatite or brushite, thereby contributing to the development of the mechanical property.[25] However, findings from an alternative study indicated that the presence of phosphate in SSA could readily adsorb onto the surface of C_3S, thereby hindering the hydration rate of cement clinker, resulting in a delay in the setting time of cement-based materials.[26]

In our previous studies, we found that varying the incineration temperatures significantly influenced the transformation of the mineral components in SSA, particularly with regard to the activity of Si/Al phase minerals.[23,27] The influence of SSA on the early hydration of cement primarily arises from the dissolution of the reactive aluminate in SSA, which is closely linked to the incineration temperature.[27] Reactive aluminates dissolved from SSA can react with portlandite and gypsum, thereby promoting the formation of ettringite and aluminum-bearing hydration products. Based on the similar physicochemical property of SSA to that of calcined clay, we previously explored the potential application of SSA to replace calcined clay in a ternary limestone calcined clay cement.[28] The findings demonstrated that incorporating 15% SSA and 7.5% limestone into mortar resulted in an enhanced compressive strength and reduced carbon emissions compared to plain cement mortar. However, there has been limited research on the influence of SSA on the hydration process and microstructural development of ternary systems incorporating SSA, cement and limestone, particularly concerning the synergistic effects between SSA and limestone. Furthermore, gypsum plays a pivotal role in the hydration of aluminates such as C_3A clinker and reactive alumina in the supplementary cementitious materials.[29] Therefore, this study investigated the hydration kinetics, phase assemblage, microstructure and mechanical performance of a ternary cementitious material. Specifically, the influence of gypsum on the hydration properties and strength development of this ternary system was examined using various characterization techniques, including isothermal calorimetry, quantitative X-ray diffraction (QXRD), thermogravimetric analysis (TGA) and BET nitrogen adsorption.

2 Experimental section

2.1 Raw materials

The Portland cement (P·I 42.5) employed in this research was manufactured by Fushun Cement Incorporated Company. The sewage sludge was acquired from a wastewater treatment plant located in Changsha. After dehydration, the sludge was dried at 105 °C for a duration of 24 h and then subjected to ball milling for 1 h. Subsequently, the powdered sludge was transferred to a high-temperature muffle furnace (KSL-1700X-A3) and subjected to calcination at 800 °C for a duration of 4 h. Fig. 1 illustrates the production process and microtopography of the incineration sludge ash. As seen in the images, the SSA particles exhibited an irregular shape with a relatively rough surface, leading to a high specific surface area.

Table 1 presents the chemical compositions and physical characteristics of the raw materials. The mineralogical composition of these materials is illustrated in Fig. 2, where quartz, muscovite and hematite could be recognized as the main minerals of SSA. The particle-size distributions of the raw materials were evaluated through laser diffraction analysis and the results are presented in Fig. S1.† Quartz powder exhibited a similar particle size to SSA, which was utilized as an inert filler

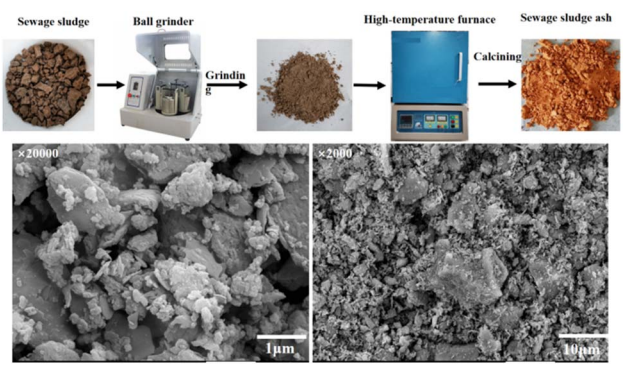

Fig. 1 Manufacturing process and microtopography of SSA.

Table 1 Chemical compositions and physical properties of raw materials

	Cement	Limestone	Quartz	Sewage sludge ash
Chemical composition (%)				
SiO_2	20.58	1.25	99.47	45.95
CaO	63.57	42.10	0.03	2.08
Al_2O_3	4.97	0.32	0.43	25.61
Fe_2O_3	3.58	0.16	0.04	8.46
MgO	2.29	7.23	—	1.51
Na_2O	0.53	—	—	0.28
K_2O	0.66	0.05	0.02	2.87
P_2O_5	—	—	—	5.93
SO_3	2.00	0.04	—	0.42
LOI (%)	1.82	42.60	0.02	1.59
Physical property				
D_{50} (μm)	14.34	19.08	13.23	10.54
Specific gravity (g cm^{-3})	3.12	2.76	2.65	2.71
BET specific surface area (m^2 g^{-1})	0.65	1.22	1.11	14.51

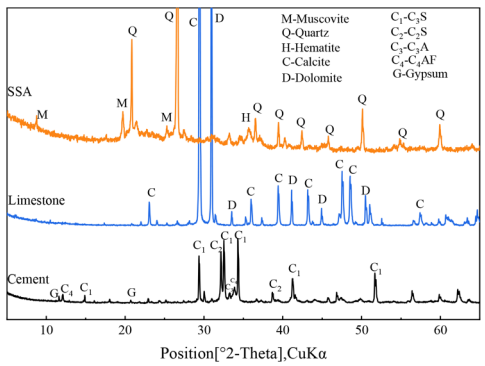

Fig. 2 XRD patterns of raw materials.

to replicate the dilution effect induced by SSA and limestone in the cement paste.

2.2 Methods

2.2.1 Sample preparation. Different cement mixtures were formulated to differentiate the impact of the individual components on the hydration, microstructure and strength development. The reference group was named OPC and consisted of 100% cement. In the other mixtures, 30% cement was replaced by quartz powder, sewage sludge ash or limestone. The phase assemblage of the ternary mixture incorporating SSA and limestone was influenced by the concentrations of alumina, sulfate and carbonate present in the mixture.[30,31] Consequently, the SLC series was formulated with an additional 1–4% gypsum to examine how the sulfate content affects cement hydration; for instance, the SLC-1 sample contained 1% gypsum. The ratios of cement, SSA, and limestone were meticulously controlled. The formulations of the blends used in this research are detailed in Table 2.

A blended paste with a water-to-binder ratio of 1 : 2 was prepared for the analysis of the hydration phase composition and for the pore-size-distribution measurements. The initial step involved blending and achieving uniformity of the raw materials using a mixer at a speed of 500 rpm for 2 min. Next, water was introduced into the mixture and stirred at 800 rpm for 90 s, followed by agitation at 1600 rpm for an additional 90 s. The blended slurries were poured into a plastic mold (40 × 40 × 40 mm) and placed in a standard curing environment maintained at a temperature of 20 °C with a relative humidity of 95%. Until the testing time, the hardened samples were sectioned into fragments and then soaked in isopropanol for a duration of 7 days to effectively halt the hydration process. Finally, the cement samples were vacuum dried for subsequent microscopic characterization. Mortar samples were prepared using identical proportions of the aforementioned paste to carry out the compressive strength tests.

2.2.2 Isothermal calorimetry. The heat evolution during the hydration of the blended cement slurry was monitored using an 8-Channel TAM Air isothermal calorimeter. All the test samples were mixed at a consistent speed and duration to minimize experimental variability. The test data were recorded over a period of 70 h at a controlled temperature of 20 °C.

2.2.3 X-ray diffraction analysis. The chemical compositions of the raw materials were determined by X-ray fluorescence (XRF) using a Bruker S4 Pioneer spectrometer. XRD analysis was conducted on a Bruker D8 Advance diffractometer at a scanning rate of 2° min^{-1} from 5° to 65° (2-theta) to examine the mineral

Table 2 Mixture proportions of the cement pastes (%)

Serials	Cement	Quartz	SSA	Limestone	Gypsum
OPC	98.0	0	0	0	2.0
QPC	68.0	30.0	0	0	2.0
SQC	68.0	10.0	20.0	0	2.0
LQC	68.0	20.0	0	10.0	2.0
SLC-1	68.7	0	20.2	10.1	1.0
SLC-2	68.0	0	20.0	10.0	2.0
SLC-3	67.3	0	19.8	9.9	3.0
SLC-4	66.6	0	19.6	9.8	4.0

compositions of the raw materials and the hydration products of the cement mixtures. Qualitative and quantitative identification of the hydration products were carried out by XRD-Rietveld analyses, employing an internal standard material (20% zincite).

2.2.4 Pore-size-distribution measurements. The pore structures of the cement samples were characterized using N_2 adsorption with an SSA-4000 (BJ-Builder) pore-size analyzer. The test samples were subjected to degassing at 40 °C for 6 h to ensure the complete removal of the gas adsorbed on the pore surfaces. The volume of nitrogen gas adsorbed was recorded over the relative pressure range (P/P_0) of 0.005 to 0.995 during both the adsorption and desorption processes. The measurement data were analyzed using the Barrett–Joyner–Halenda (BJH) model, considering a pore-size distribution from 2 nm to 100 nm.

2.2.5 Scanning electron microscopy analysis. The morphology and backscattered electron micrograph (BSE) of hardened cement paste were observed using a scanning electron microscopy system (SEM; QUANTA FEG250) with an accelerating voltage of 15 kV. BSE images were also obtained to analyze the microscopic appearance of different hydrated phases in the cement paste and the reaction degree of the cement clinker.

2.2.6 Compressive strength. The compressive strengths of the mortars were evaluated using a uniaxial pressure testing apparatus (Testometric X500-50) with a loading rate of 2.40 kN s^{-1} at 1 day, 3 days, 7 days, 28 days and 90 days. Three specimens were tested and the average value was taken from these tests to obtain the compressive strength.

3 Results and discussion

3.1 Reaction kinetics at an early age of hydration

The hydration heat flow curves of cement pastes, normalized to the cement content, over a curing duration of 72 h are presented in Fig. 3. As depicted in Fig. 3a, there were three peaks on the heat flow curves for all the cement pastes, while an obvious third shoulder peak occurred in the paste with the incorporation of SSA (such as SQC and SLC-2). The first peak (denoted as I) was identified as the hydration peak of aluminate clinker (C_3A), and ettringite forms in the presence of gypsum during this phase. Due to the rapid reaction at this phase, we knew there were bound to be some measurement errors after inserting the sample into the calorimeter. Therefore, the slight differences in the first phase are not the focus of this discussion. The second peak (marked as II) corresponded to the silicate clinker (C_3S) hydration peak. Compared to the reference OPC paste, the incorporation of quartz powder, SSA and limestone led to an augmented initial release of the hydration heat. The QPC and LQC pastes exhibited a shorter time for the induction period and a higher intensity of peak II than the OPC paste. On the one hand, the filler effect of the fine quartz and limestone particles provided a large number of crystal nuclei for the crystallization and precipitation of the C–S–H gel and portlandite, accelerating the hydration process of the clinker.[32] On the other hand, the additional Ca^{2+} ions dissolved from limestone accelerated the hydration of the cement clinker, particularly for C_3S, and thereby shortened the induction period.[33] Similarly, the fine SSA particles also exhibited an accelerated effect on cement hydration as presented in the SQC and SLC-2 paste cases. The SQC paste exhibited a maximum heat flow of 3.13 mW g^{-1}, which was 16.4% higher than that of the reference group. The third shoulder peak (marked as III) during the deceleration period resulted from the reaction of SSA in this blended system.[34] The third peaks observed in the SQC and SLC-2 paste were significantly elevated compared to those of the other groups, which was attributed to the incorporation of SSA. It has been demonstrated that SSA provides additional reactive aluminate and silicate to hydrating cement systems, thereby facilitating the formation of aluminum-containing hydration products, such as ettringite and C–A–S–H gel.[35] The reaction of SSA at this stage will be addressed in later sections of this paper in accordance with the evolution of the phase assemblage in the blended ternary system.

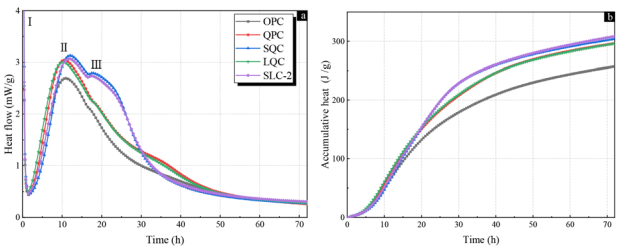

Fig. 3 Isothermal calorimetry and cumulative heat release curves of blended pastes: (a) heat flow and (b) cumulative heat release. Notes: all data were normalized to the amount of cement.

The cumulative heat curves of the cement pastes, normalized to the cement content over a curing period of 72 h, are presented in Fig. 3b. It was demonstrated that the inclusion of quartz, SSA, and limestone accelerated the hydration of cement clinker, resulting in a marked increase in cumulative heat compared to the controlled OPC group. The QPC and LQC pastes presented similar growth trends in the cumulative heat curves, as a result of the low reactivity of limestone at an early age of cement hydration. The SQC and SLC-2 pastes with the incorporation of SSA exhibited lower cumulative heat at the initial hydration stage compared to the QPC paste. Interestingly, it increased rapidly after 20 h of hydration, as can be seen in Fig. 3b. The accelerated growth observed in the cumulative heat curves of these two groups corresponds to the third peaks depicted in Fig. 3a, taking into account the reaction of SSA. At 72 h, the cumulative heat in the SLC-2 paste reached 308.3 J g^{-1}, a significant increase of 19.8% compared with the reference paste. It can be concluded that the interaction of SSA, limestone and cement within the ternary system generated the additional hydration heat.

The hydration heat flow of the ternary blended system incorporating SSA and limestone with varying gypsum contents was normalized to the cement content, and the results are presented in Fig. 4a. During the induction and acceleration period of cement hydration, all the ternary pastes showed a similar rate of hydration heat evolution. This indicated that

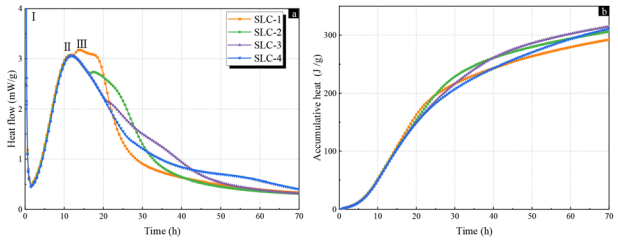

Fig. 4 Isothermal calorimetry and cumulative heat release curves of SLC paste with different gypsum contents: (a) heat flow and (b) cumulative heat release.

the intensity and occurrence time of the induction period and acceleration period of ternary hydration was not influenced by the gypsum content. However, after reaching the second exothermic peak of cement hydration, the gypsum content exerted a delayed influence on the follow-up hydration process. The SLC-1 paste with 1% gypsum exhibited the III exothermic peak at 14 h of hydration, which was delayed by 3.5 and 7.5 h comparted to the SLC-2 and SLC-3 pastes. Furthermore, the magnitudes of the III peak in the other pastes were also decreased. The SLC-4 paste with the addition of 4% gypsum presented a gentle slope instead of the III peak. As above-mentioned for Fig. 3a, this exothermic peak corresponded to the reaction of active aluminate and silicate in SSA with cement.[35] The delayed impact of gypsum on the hydration of SSA was attributed to the reaction between sulfate ions and aluminates in the SSA.[36] The accumulative hydration heat of the ternary system, normalized to the cement content within a curing period of 72 h, is illustrated in Fig. 4b. It could been seen that the accumulative heat of the SLC-1 paste was higher than that of the other groups during the first 24 h of hydration. However, it increased moderately and was surpassed by the other groups after 24 h. At the hydration age of 70 h, the SLC-1 paste presented a cumulative heat of 292.5 J g^{-1}, and the cumulative heat became elevated with the increasing gypsum content. The SLC-3 paste with 3% gypsum reached 314.8 J g^{-1}, representing a significant increase of 7.6% compared to that of SLC-1. As hydration progressed, the cumulative heat of the SLC-4 paste exhibited a trend nearly surpassing that of SLC-3. It was therefore clearly evident that the incorporation of additional gypsum resulted in an increase in the cumulative heat of this ternary system, attributable to its reaction with the aluminates present in SSA.

3.2 Hydration phase assemblage

The XRD patterns of various cement samples at curing ages of 1 day, 3 days, 7 days and 28 days, are shown in Fig. 5. As can be seen in this figure, all the samples at the age of 1 day presented predominant hydration products, such as portlandite (2θ = 18.1°), ettringite (2θ = 9.1°) and unhydrated clinkers. The differences in the intensity of the characteristic peaks point out that the contents of the various hydration products were different from each other, which is discussed in a later section. At 3 days of hydration, the characteristic peak of C_3S could still be observed in the reference OPC, while it had disappeared for

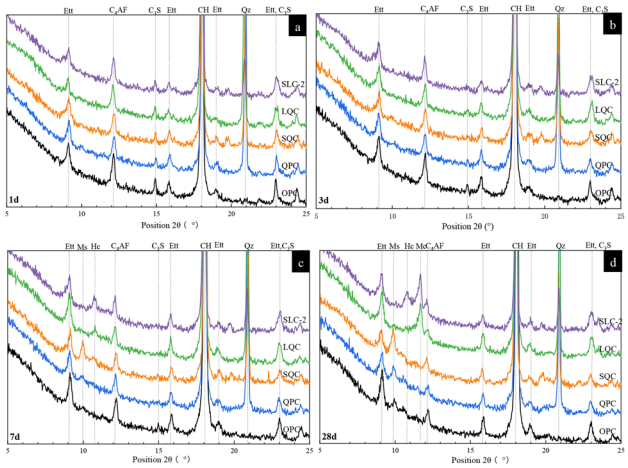

Fig. 5 XRD patterns of cement paste at various curing times: (a) 1 day, (b) 3 days, (c) 7 days, and (d) 28 days. Notes: Ett-ettringite, Ms-monosulfate, CH-portlandite, Hc-hemicarboaluminate, Mc-monocarboaluminate, and Qz-quartz.

the other pastes. This discrepancy could be attributed to the accelerating effects of SSA, quartz and limestone on the hydration degree of C_3S clinker. Here, as sulfate in the cement paste is depleted, ettringite begins to transform into monosulfate. As shown in Fig. 5c, the characteristic peak of monosulfate (2θ = 10.0°) could be observed in the XRD patterns of all the samples except for the LQC and SLC-2 pastes. In these two pastes blended with limestone, a distinct peak corresponding to a hemicarboaluminate (2θ = 10.8°) phase was noted at the hydration age of 7 days, attributed to the presence of carbonate sources in the system. The SQC paste exhibited the highest intensity monosulfate peak since the large quantities of alumina available from SSA promoted the transformation of ettringite into monosulphate. As the hydration reaction progressed, the peak intensity of ettringite decreased, while the peak intensity of monosulfate increased in the XRD patterns of the OPC, QPC and SQC pastes at 28 days. The full conversion of hemicarboaluminate to monocarboaluminate (2θ = 11.7°) was monitored in LQC paste after 28 days. In the limestone-blended system, the monocarboaluminate phase was more stable than the hemicarboaluminate phase, as determined by the calculation of the Gibbs energy minimization.[37] Despite the abundant carbonate sources available in the system for the formation of hydrated carboaluminate phases, only a partial transformation of the hemicarboaluminate phase was detected in the SLC-2 blend paste. The reactivity of calcite has been shown to be affected by the levels of alumina and sulfate in ternary LC^3 systems.[38] Additionally, a minor peak of hemicarboaluminate was observed in the OPC and QPC samples, which may be attributed to carbonation of the sample during the XRD test.

Quantitative phase analysis of various hydration products was carried out by the XRD-Rietveld method and the results are presented in Fig. 6. As illustrated in Fig. 6a, with the incorporation of quartz, limestone and SSA, the portlandite contents of the test samples were higher than that of the control sample OPC in the first 24 h of hydration, resulting from the

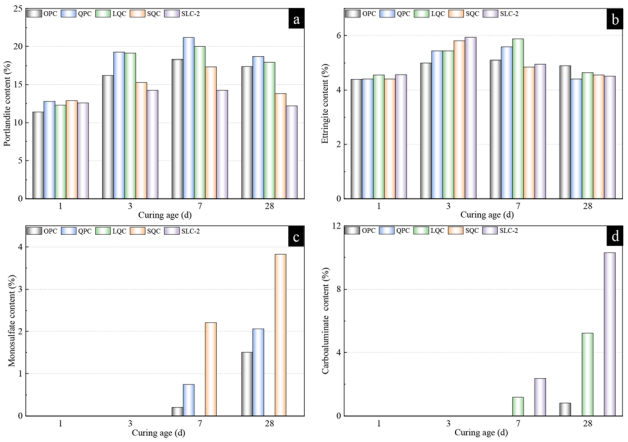

Fig. 6 Hydration product content of cement paste calculated by the XRD-Rietveld method: (a) portlandite, (b) ettringite, (c) monosulfate, and (d) carboaluminate.

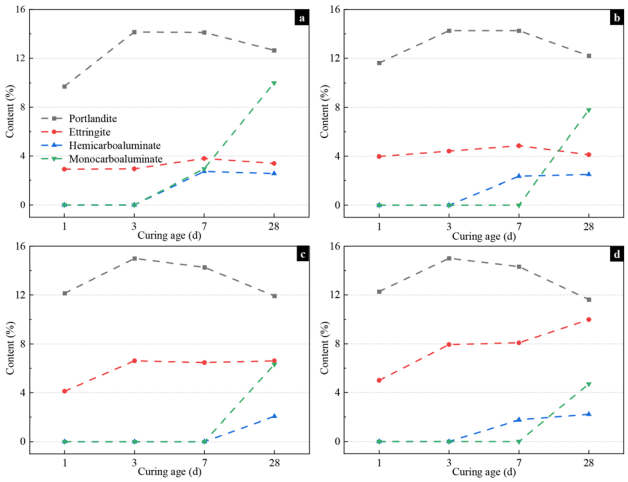

Fig. 7 Hydration product content of SLC paste with different gypsum contents calculated by XRD-Rietveld analysis: (a) 1% gypsum, (b) 2% gypsum, (c) 3% gypsum, and (d) 4% gypsum.

accelerating effect of these additives on C_3S hydration. The portlandite contents in all the samples increased in the first 7 days with the hydration of cement clinkers. In comparison to the OPC sample, a notable reduction in portlandite content was noted in the SQC and SLC-2 samples after 3 days of hydration, which coincided with the increases in ettringite content in these two samples. This illustrated that the additional ettringite was produced from the reaction between aluminate in SSA and portlandite within the system. The SLC-2 paste exhibited the highest ettringite content of 5.93% among all the cement pastes at age of 3 days. The transformation of the ettringite phase to monosulfate or carboaluminate phase occurred after 7 days of hydration, resulting in an increase in monosulfate content and a corresponding decrease in ettringite content, as shown in Fig. 6b. The monosulfate content in the SQC paste at 28 days was 3.82%, compared to only 1.50% in the reference OPC paste. Considering the reactions of limestone, the hydrated carboaluminate content, including the hemicarboaluminate and monocarboaluminate phases, was significantly increased at 28 days in the LQC and SLC-2 pastes, reaching up to 5.21% and 10.29%, respectively.[39,40]

The influence of gypsum on the hydration phase assemblage in the ternary blended system containing limestone and SSA is shown in Fig. S2,† while the quantify analysis based on the XRD patterns is illustrated in Fig. 7. It is evident from XRD patterns that the predominant hydration products observed in all the samples were ettringite, portlandite and undetected C–S–H gel at the hydration age of 1 day and 3 days. Moreover, the peak intensity of the ettringite phase was augmented with increasing the gypsum content at all ages, which corresponded to a rise in ettringite content. The characteristic peak of gypsum was still evident in the XRD pattern of SLC-4 at 1 day but had disappeared after 3 days of hydration, which means that 4% added gypsum was superfluous for this ternary system. After 7 days of hydration, the XRD patterns of the samples with 1–3% gypsum exhibited the characteristic peak of the hemicarboaluminate phase, which was not observed in SLC-4. The peak intensity of the ettringite phase increased with the rising gypsum content, whereas the intensities of the hemicarboaluminate and monocarboaluminate phases exhibited an inverse correlation at 28 days of hydration. Evidently, the addition of gypsum promoted the formation of the ettringite phase while hindering its transformation to the carboaluminate phase.[41] As illustrated in Fig. 7d, the ettringite content in the SLC-4 sample increased from 5% to 10% at 1 day and 28 days of hydration. However, the content of the carboaluminate phase decreased with the increasing gypsum content after 7 days of hydration. The contents of the hemicarboaluminate and monocarboaluminate phases in the SLC-1 paste were measured as 2.5% and 10.0% at 28 days, respectively, compared to 2.0% and 4.7% in the SLC-4 paste.

As discussed above, the primary hydration products of the ternary system incorporating SSA and limestone included portlandite, ettringite, monosulfate, carboaluminates, and amorphous C–S–H gel. Initially, the C_3A clinker and aluminates in SSA reacted with gypsum ($C\$H_2$) to form the ettringite ($C_6A\$_3H_{32}$) phase. Subsequently, the ettringite phase began to transform into monosulfate ($C_4A\$H_{12}$) under the condition of gypsum depletion. The presence of limestone facilitated the reaction between the monosulfate and carbonate ions within the ternary system, leading to the formation of ettringite and hydrated carboaluminate phases.[31,32,39] Furthermore, the additional gypsum promoted the formation of ettringite but delayed the transformation of ettringite to the carboaluminate phase. The hydration reactions can be represented by the following equations (eqn (1)–(4)).

$$3C\$H_2 + C_3A + 26H \rightarrow C_6A\$_3H_{32} \quad (1)$$

$$C_6A\$_3H_{32} + 2C_3A + 4H \rightarrow 3C_4A\$H_{12} \quad (2)$$

$$3C_4A\$H_{12} + 2C\bar{C} + 18H \rightarrow C_6A\$_3H_{32} + 2C_4A\bar{C}H_{11} \quad (3)$$

$$C_3A + C\bar{C} + 11H \rightarrow C_4A\bar{C}H_{11} \quad (4)$$

Carboaluminate hydrate phases are commonly found in cement pastes containing limestone, including hemicarboaluminate ($C_4A\bar{C}_{0.5}H_{12}$) and monocarboaluminate ($C_4A\bar{C}H_{11}$). Hemicarboaluminate is regarded as a metastable phase, whereas monocarboaluminate has been identified as the stable phase in cement paste, as indicated by thermodynamic simulation results in various studies.[42,43] As previously reported, the stability of hydrated carboaluminolates is contingent upon the content of CO_3^{2-}, SO_3 and Al_2O_3 in the cement paste.[37] In the ternary system incorporating SSA and limestone, SSA provides reactive aluminosilicate, while limestone contributes CO_3^{2-} ions that participate in the hydration reactions of cement clinkers. The supplementary hydration products arising from this process are essential for improving the microstructure and mechanical properties of the ternary system.

3.3 Microstructure evolution

To characterize the influence of SSA, quartz and limestone on the pore structure of the cement samples, the pore-size distributions of the samples were determined using a nitrogen-adsorption instrument, as illustrated in Fig. 8. There were notable variations in pore distribution among the different samples. As depicted in Fig. 8a, the QPC paste containing 30% quartz powder exhibited the highest overall pore volume. Moreover, the pore volume of LQC paste with 20% quartz and 10% limestone powder surpassed that of the reference OPC paste. The observed increase in pore volume could be attributed to the inert nature and diluting effect of quartz and limestone within the cement paste. In contrast, the incorporation of SSA, such as in the SQC and SCL-2 samples, led to a reduction in pore volume when compared to the reference pastes. This observation indicates that the hydration products formed from the reaction among SSA, cement, and limestone could effectively permeate into the pores, resulting in a substantial reduction in the total pore volume.

The pore structure in cement paste can be classified into four categories according to the pore size: gel pores (<4.5 nm), medium pores (4.5–50 nm), medium capillary pores (50–100 nm) and large capillary pores (>100 nm). Fig. 8b illustrates the relative proportions of each pore size in relation to the total pore volume. In the reference OPC paste, the gel pore volume accounted for 9.4%, while the middle pore constituted the majority at approximately 70.9%. The medium and large capillary pores comprised 15.7% and 4.1%, respectively. The proportions of large capillary pores in the QPC and LQC pastes were 5.3% and 7.9%, respectively. Consequently, due to the filling effect of additional hydrated products, the proportion of gel pores in the SLC-2 paste rose to 35.8%, while the medium and large capillary pores accounted for only 1.8%.

The pore volume distributions of the samples with varying gypsum contents are illustrated in Fig. 9. As depicted in Fig. S3,† the overall pore volume of cement paste exhibited a decrease as the gypsum content increased. Notably, the SLC-3 paste containing 3% gypsum demonstrated the minimum pore volume. However, the total pore volume increased when the gypsum content exceeded 3%. It is clear from Fig. 9 that the proportion of gel pores escalated with increasing the gypsum content, reaching 10.9% and 36.3% in the SLC-0 and SLC-4 pastes, respectively. The synergic effect of SSA, limestone and gypsum refined the pore structure of cement paste, resulting in a significant reduction in the proportion of large capillary pores from 4.2% in the SLC-0 paste to 0.5% in the SLC-4 paste. The findings also demonstrated that additional gypsum (exceeding 3%) did not contribute to the hydration reactions of sludge ash and limestone, thereby resulting in an elevation of the total porosity.

The SEM and BSE images of the reference (OPC) and blended pastes incorporating SSA and limestone are shown in Fig. 10. As observed in the SEM image of the reference, various hydration products were crosslinked together to form a three-dimensional network structure (Fig. 10a). With the addition of limestone, some discernible pores and microcracks were observed in the LQC paste (Fig. 10c). Compared to the reference paste, the SLC-2 paste incorporating SSA presented a more compact structure as

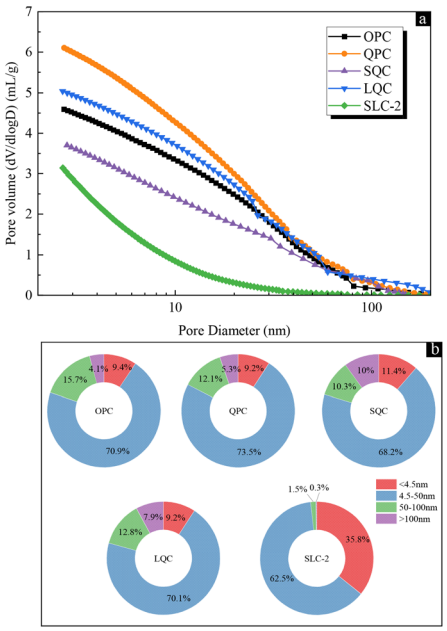

Fig. 8 (a) Pore volume distributions and (b) relative proportions of each pore size in the cement paste with various compositions.

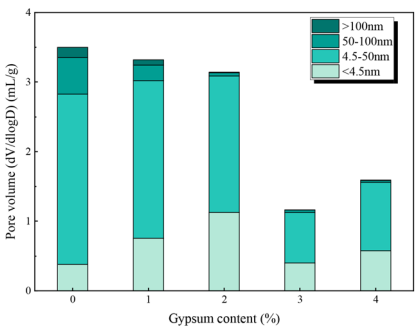

Fig. 9 Proportions of each pore size in SLC-2 paste with various gypsum contents.

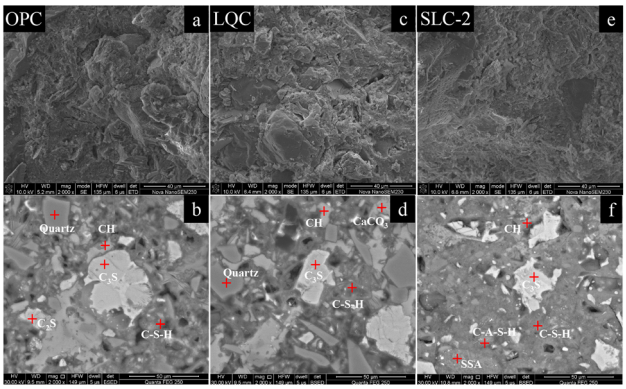

Fig. 10 SEM and BES images of cement paste at 28 days: (a and b) OPC paste, (c and d) LQC paste, and (e and f) SLC-2 paste.

a result of the filling effect of additional hydration products and fine SSA particles (Fig. 10e). The phase assemblages in the BSE image could be approximately identified by the gray levels based on their mean atomic weight. In Fig. 10e, the dark areas are pores and cracks in the cement paste, while the brightest parts are unhydrated clinkers, such as C_3S and C_2S, followed by hydration products; for example, portlandite, C–S–H gel, or ettringite. These hydration phases were verified by EDS analysis, as appended in the ESI (Fig. S4).† It is worth noting that fewer pores and microcracks were observed in the SLC-2 paste. In this ternary blend, the interaction between the sludge ash, portlandite, and limestone facilitated the formation of additional hydration products, such as C–A–S–H gel and carboaluminate hydrates. These products can fill pores and microcracks in the paste, thereby contributing to the development of a denser microstructure. This phenomenon was consistent with the analysis of the BET pore-size distribution of the mixtures.

3.4 Compressive strength development

The mechanical property of concrete with the mineral admixture is a crucial evaluation index for engineering applications. In this section, the compressive strengths of the cement samples were evaluated at various curing ages, as illustrated in Fig. 11. The compressive strength of the reference OPC paste was recorded at 18.67, 29.50 and 52.39 MPa for curing ages of 3, 7, and 28 days, respectively. However, when quartz powder replaced cement by a proportion of 30%, the compressive strength decreased to 38.24 MPa at 28 days. The strength activity index (SAI) is determined by calculating the ratio of the compressive strength between cement paste with a 30% admixture and the reference paste containing 100% cement. This index serves as a valuable tool for assessing the pozzolanic activity of supplementary cementitious materials.[44,45] For instance, the 28-day SAI of the QPC paste exceeded the theoretical value (70%) with a measurement of 72.99%. XRD analysis revealed the absence of new hydration products in the QPC paste, indicating that the inclusion of fine quartz powder positively influenced the compressive strength development. Besides the physical filling effect provided by fine particles, the synergistic chemical interaction between SSA and limestone significantly enhanced the mechanical properties of the ternary system. Consequently, the 28-day compressive strength of SLC-2 paste, which contained 20% SSA and 10% limestone, reached 49.54 MPa with a SAI of 94.56%.

The compressive strengths of the SLC series of pastes with varying gypsum contents are presented in Fig. 12. The compressive strengths of SLC-0 paste without gypsum at 3, 7 and 28 days were recorded as 12.33, 21.88, and 41.86 MPa, respectively. Moreover, an increase in the SAI value was observed with curing age; for instance, it reached 66.03% at 3 days and further increased to 79.90% at 28 days. The synergistic effect of SSA and limestone was enhanced with the prolongation of the curing age. Additionally, the compressive strength of the specimens was improved at all ages with increasing the gypsum content, as demonstrated in Fig. 12. The 28-day compressive strength of the paste increased from 46.54 MPa to 49.54 MPa with SAI values of 88.84% and 94.56%, respectively, when the gypsum content was varied from 1% to 3%. However, the compressive strength exhibited a decline (SAI of 85.77%) with a further increase in gypsum content to 4%. The hydration heat curve of cement pastes in Fig. 4 clearly exhibited a distinct reaction peak corresponding to the gypsum component. Determination of the optimal gypsum content for the cement paste can be achieved through test analysis of the hydration heat. As demonstrated in Fig. 4, the increase in gypsum content resulted in a corresponding rise in hydration heat during the

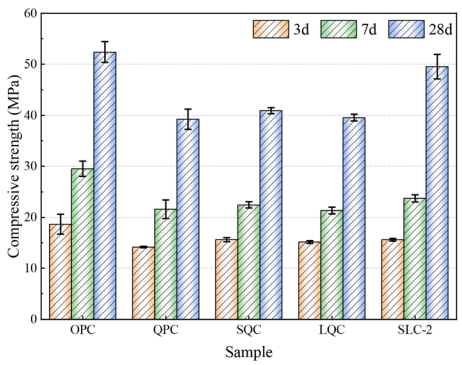

Fig. 11 Compressive strength of cement paste at various curing ages.

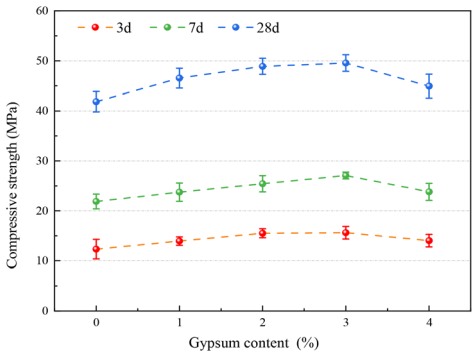

Fig. 12 Influence of gypsum content on the compressive strength of SLC series paste.

first 72 h. However, it should be noted that the rate of growth in hydration heat decreased when the gypsum content exceeded 3%. In relation to the hydration heat, the compressive strength of the specimens initially increased and subsequently decreased with the rising gypsum content. The maximum strength value of cement paste was achieved at a gypsum content of 3%. Therefore, based on the findings related to the hydration heat and compressive strength, the optimal gypsum content for the SLC paste was identified as 3%.

The strength contribution of supplementary cementitious materials to cement paste primarily arises from the effects of physical filling and chemical reactions.[46] Consequently, the compressive strength of this ternary system can be categorized into three components: cement hydration, physical filling, and chemical reaction of SSA and limestone. The compressive strength of the SLC-3 paste containing 20% sludge ash and 10% limestone at different ages was tested and analyzed to accurately quantify the synergistic effect of both two admixtures on strength development. Here, the strength resulting from cement hydration (S_{ch}) was calculated as 70% of the compressive strength (S_{OPC}) of cement paste with 100% cement, while the strength provided by physical filling (S_{pf}) was calculated by the strength (S_{QPC}) of the QPC paste with 30% quartz powder subtracting S_{ch}, and the strength arising from the chemical reaction of sludge ash and limestone (S_{cr}) was obtained from the strength of the SLC-3 paste (S_{SLC}) subtracting S_{ch} and S_{pf}. The parameters were computed according to the following equations (eqn (5)–(7)), and the corresponding results are presented in Fig. 13.

$$S_{ch} = 0.7 \cdot S_{OPC} \quad (5)$$

$$S_{pf} = S_{QPC} - S_{ch} \quad (6)$$

$$S_{cr} = S_{SLC} - S_{ch} - S_{pf} \quad (7)$$

The data indicated a rise in absolute compressive strength attributed to the cement hydration and chemical reactions as the curing age increases. For instance, the S_{ch} and S_{cr} values of the SLC-3 paste increased from 9.68 MPa and 0.63 MPa to 38.97 MPa and 12.80 MPa, respectively, as the curing age progressed from 1 day to 90 days. The results indicated the continuous presence of cement hydration and the reaction of each component in the cement paste throughout the whole curing period. The pie charts in Fig. 13 present the ratios of compressive strength contributed by the three distinct effects at different ages. This figure illustrates that the strength ratios of the cement hydration and physical filling effects were 86.05% and 8.35% at 1 day, respectively, while the strength contribution from chemical reaction was only 5.60%. Consequently, during the initial stage of hydration within 7 days, the mechanical strength of the cement sample primarily originated from the effect of cement hydration and physical filling. The contribution ratio of the cement hydration and physical filling effects to the strength development decreased with increasing the curing age, while the proportion of strength provided by the chemical reactions effect increased from 5.60% at 1 day to 24.20% at 90 days. The mechanical strength of cement paste during the later stages of hydration could be attributed to cement hydration and chemical reactions among the various components. This indicated that the incorporation of SSA and limestone in the ternary system can enhance the strength development of hardened cement paste.

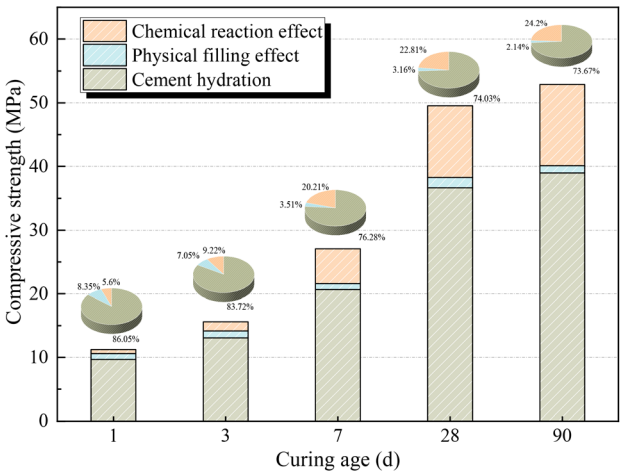

Fig. 13 Compressive strength value and ratio provided by cement hydration, physical filling and chemical reaction effects.

4 Conclusions

This study investigated the synergistic effects of sewage sludge ash and limestone on the hydration kinetics, phase assemblage and mechanical property of ternary cement-based composites. The results showed that the incorporation of SSA and limestone provided abundant crystal nuclei for the crystallization and precipitation of hydration products, thereby accelerating the early hydration of the cement and enhancing the cumulative heat release. The reaction between SSA and limestone facilitated the formation of hydrated carboaluminate phases and refined the pore structures of the ternary composites. Furthermore, gypsum was used to optimize the mechanical property of the ternary composites and the optimal gypsum content was determined to be 3% according to the performance related to the hydration heat and compressive strength. Based on these results, this study proposes an alternative path for the utilization of solid wastes (SSA and limestone) in the production of construction materials. Further research will focus on examining the long-term durability, such as sulfate resistance, dry shrinkage and freeze–thaw resistance, of the ternary cement-based composites.

Data availability

All data supporting the findings of this study are available upon request.

Author contributions

Zhiyang Chang: conceptualization, methodology, data curation, and writing – original draft. Huimin Wang: tests and data

curation. Hongzhi Yue: tests and data curation. Huijun Xu: conceptualization, resources, and polishing – original draft. Dongming Liu: supervision and resources.

Conflicts of interest

There are no conflicts to declare.

Acknowledgements

The authors gratefully acknowledge financial support from the Natural Science Foundation of Shandong Province (No. ZR2023QE219 and ZR2022QB012) and Innovation Capability Enhancement Project for Technology-based Small and Medium-sized Enterprises of Shandong Province (No. 2024TSGC0488 and 2023TSGC0968).

Notes and references

1 P. Fennell, J. Driver, C. Bataille and S. J. Davis, *Nature*, 2022, **603**(7902), 574–577.
2 X. Liu, L. Yang, J. Du, H. Zhang, J. Hu, A. Chen and L. Wei, *Resour., Conserv. Recycl.*, 2024, **204**, 107498.
3 V. Pitre, H. La and J. A. Bergerson, *J. Cleaner Prod.*, 2024, **475**, 143717.
4 O. Cavalett, M. D. B. Watanabe, M. Voldsund, S. Roussanaly and F. Cherubini, *Nat. Sustainable*, 2024, **7**(5), 568–580.
5 M. G. Plaza, S. Martínez and F. Rubiera, *Energies*, 2020, **13**(21), 5692.
6 M. Georgiades, I. H. Shah, B. Steubing, C. Cheeseman and R. J. Myers, *Resour., Conserv. Recycl.*, 2023, **194**, 106998.
7 I. H. Shah, S. A. Miller, D. Jiang and R. J. Myers, *Nat. Commun.*, 2022, **13**(1), 5758.
8 F. Avet, R. Snellings, A. A. Diaz, M. B. Haha and K. Scrivener, *Cem. Concr. Res.*, 2016, **85**, 1–11.
9 Y. Dhandapani and M. Santhanam, *Cem. Concr. Res.*, 2020, **129**, 105959.
10 Y. Dhandapani, T. Sakthivel, M. Santhanam, R. Gettu and R. G. Pillai, *Cem. Concr. Res.*, 2018, **107**, 136–151.
11 C. Liew, W. Kiatkittipong, J. Lim, M. Lam, Y. Ho, C. Ho, S. K. O. Ntwampe, M. Mohamad and A. Usman, *Chemosphere*, 2021, **277**, 130310.
12 M. Schnell, T. Horst and P. Quicker, *J. Environ. Manage.*, 2020, **263**, 110367.
13 H. Chang, Y. Zhao, V. Bisinella, A. Damgaard and T. H. Christensen, *Water Res.*, 2023, **240**, 120109.
14 Z. Chang, G. Long, J. L. Zhou and C. Ma, *Resour., Conserv. Recycl.*, 2020, **154**, 104606.
15 S. De Carvalho Gomes, J. L. Zhou, W. Li and G. Long, *Resour., Conserv. Recycl.*, 2019, **145**, 148–159.
16 S. Guo, R. Dong, Z. Chang, Y. Xie, G. Chen and G. Long, *Constr. Build. Mater.*, 2023, **367**, 130028.
17 Y. Xia, M. Liu, Y. Zhao, J. Guo, X. Chi, J. Du, D. Du and D. Shi, *Sci. Total Environ.*, 2023, **864**, 161116.
18 T. Zdeb, T. Tracz and M. Adamczyk, *J. Cleaner Prod.*, 2022, **345**, 131055.
19 W. Piasta and M. Lukawska, *Procedia Eng.*, 2016, **161**, 1018–1024.
20 Y. Xia, M. Liu, Y. Zhao, X. Chi, Z. Lu, K. Tang and J. Guo, *J. Environ. Manage.*, 2023, **326**, 116690.
21 C. Gu, Y. Ji, J. Yao, Y. Yang, J. Liu, T. Ni, H. Zhou, Y. Tong and X. Zhang, *Constr. Build. Mater.*, 2022, **318**, 125823.
22 S. Chakraborty, B. W. Jo, J. H. Jo and Z. Baloch, *J. Cleaner Prod.*, 2017, **153**, 253–263.
23 Z. Chang, G. Long, Y. Xie and J. L Zhou, *Constr. Build. Mater.*, 2022, **318**, 126096.
24 S. Donatello, A. Freeman-Pask, M. Tyrer and C. R. Cheeseman, *Cem. Concr. Compos.*, 2010, **32**(1), 54–61.
25 M. Mejdi, M. Saillio, T. Chaussadent, L. Divet and A. Tagnit-Hamou, *Cem. Concr. Res.*, 2020, **135**, 106115.
26 K. L. Scrivener and A. Nonat, *Cem. Concr. Res.*, 2011, **41**(7), 651–665.
27 Z. Chang, G. Long, Y. Xie and J. L. Zhou, *Constr. Build. Mater.*, 2022, **322**, 126116.
28 Z. Chang, G. Long, Y. Xie and J. L. Zhou, *J. Build. Eng.*, 2022, **49**, 104035.
29 S. Adu-Amankwah, L. Black, J. Skocek, M. B. Haha and M. Zajac, *Constr. Build. Mater.*, 2018, **164**, 451–462.
30 Y. Liu, Y. Zhuge, C. W. K. Chow, A. Keegan, P. N. Pham, D. Li, J. Oh and R. Siddique, *Resour., Conserv. Recycl.*, 2021, **168**, 105291.
31 E. Qoku, T. A. Bier, G. Schmidt and J. Skibsted, *Cem. Concr. Compos.*, 2022, **131**, 104502.
32 Y. Briki, M. Zajac, M. B. Haha and K. Scrivener, *Cem. Concr. Res.*, 2021, **147**, 106515.
33 E. Berodier and K. Scrivener, *J. Am. Ceram. Soc.*, 2014, **97**(12), 3764–3773.
34 Y. Xia, M. Liu, Y. Zhao, X. Chi, J. Guo, D. Du and J. Du, *Constr. Build. Mater.*, 2023, **375**, 130868.
35 J. Zhou, K. Zheng, Z. Liu and F. He, *Cem. Concr. Res.*, 2019, **116**, 159–167.
36 Y. Xia, Y. Zhao, M. Liu, J. Guo, J. Du and D. Du, *Constr. Build. Mater.*, 2023, **364**, 129982.
37 M. Zajac, A. Rossberg, G. Le Saout and B. Lothenbach, *Cem. Concr. Compos.*, 2014, **46**, 99–108.
38 M. Zajac, P. Durdzinski, C. Stabler, J. Skocek, D. Nied and M. B. Haha, *Cem. Concr. Res.*, 2018, **106**, 91–102.
39 Y. Dhandapani, M. Santhanam, G. Kaladharan and S. Ramanathan, *Cem. Concr. Res.*, 2021, **143**, 106396.
40 T. Matschei, B. Lothenbach and F. P. Glasser, *Cem. Concr. Res.*, 2007, **37**(4), 551–558.
41 H. Minard, S. Garrault, L. Regnaud and A. Nonat, *Cem. Concr. Res.*, 2007, **37**(10), 1418–1426.
42 B. Lothenbach and F. Winnefeld, *Cem. Concr. Res.*, 2006, **36**(2), 209–226.
43 T. Matschei, B. Lothenbach and F. P. Glasser, *Cem. Concr. Res.*, 2007, **37**(10), 1379–1410.
44 Y. Liu, S. Lei, M. Lin, Y. Li, Z. Ye and Y. Fan, *Appl. Clay Sci.*, 2017, **143**, 159–167.
45 A. Tironi, M. A. Trezza, A. N. Scian and E. F. Irassar, *Cem. Concr. Compos.*, 2013, **37**, 319–327.
46 Y. Sun, K. Q. Wang and H. S. Lee, *Constr. Build. Mater.*, 2021, **271**, 121532.